

Neural Representation of Shape-Dependent Laplacian Eigenfunctions

YUE CHANG, University of Toronto, Canada

OTMAN BENCHEKROUN, University of Toronto, Canada

MAURIZIO M. CHIARAMONTE, Meta Reality Labs Research, USA

PETER YICHEN CHEN, MIT CSAIL, USA

EITAN GRINSPUN, University of Toronto, Canada

The eigenfunctions of the Laplace operator are essential in mathematical physics, engineering, and geometry processing. Typically, these are computed by discretizing the domain and performing eigendecomposition, tying the results to a specific mesh. However, this method is unsuitable for continuously-parameterized shapes.

We propose a novel representation for eigenfunctions in continuously-parameterized shape spaces, where eigenfunctions are spatial fields with continuous dependence on shape parameters, defined by minimal Dirichlet energy, unit norm, and mutual orthogonality. We implement this with multilayer perceptrons trained as neural fields, mapping shape parameters and domain positions to eigenfunction values.

A unique challenge is enforcing mutual orthogonality with respect to causality, where the causal ordering varies across the shape space. Our training method therefore requires three interwoven concepts: (1) learning n eigenfunctions concurrently by minimizing Dirichlet energy with unit norm constraints; (2) filtering gradients during backpropagation to enforce causal orthogonality, preventing earlier eigenfunctions from being influenced by later ones; (3) dynamically sorting the causal ordering based on eigenvalues to track eigenvalue curve crossovers.

We demonstrate our method on problems such as shape family analysis, predicting eigenfunctions for incomplete shapes, interactive shape manipulation, and computing higher-dimensional eigenfunctions, on all of which traditional methods fall short.

CCS Concepts: • Computing methodologies → Physical simulation; Shape analysis.

Additional Key Words and Phrases: neural fields, physics simulation, geometry processing

1 INTRODUCTION

The eigenfunctions of the Laplace operator are fundamental to mathematical physics, engineering, and geometry processing, with applications to solving partial differential equations (PDEs), wave propagation, heat conduction, shape analysis, shape matching, surface parameterization, and model reduction.

For a general domain with a boundary, the common approach is to discretize the domain and eigenanalyze the discrete operator. This inextricably ties the analysis to a specific mesh, with the eigenfunctions represented in terms of mesh degrees of freedom. However, when eigenanalysis is desired for *continuously-parameterized shapes*, using a single mesh may be neither desirable nor possible.

Contributions. We propose the first eigenanalysis algorithm and eigenfunction representation specifically geared for continuously-parameterized shape spaces. For us, eigenfunctions are spatial fields

Authors' addresses: Yue Chang, University of Toronto, Canada, changyue.chang@mail.utoronto.ca; Otman Benchekroun, University of Toronto, Canada, otman.benchekroun@mail.utoronto.ca; Maurizio M. Chiaramonte, Meta Reality Labs Research, USA, mchiaram@meta.com; Peter Yichen Chen, MIT CSAIL, USA, pyc@csail.mit.edu; Eitan Grinspun, University of Toronto, Canada, eitan@cs.toronto.edu.

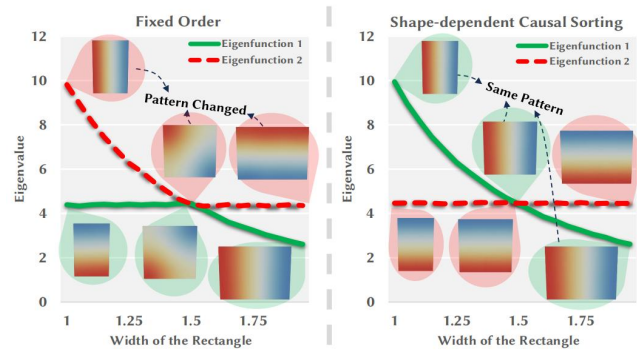


Fig. 1. Consider a family of rectangular domains $\{\Omega_g\}$, all of height=1.5, and width g . As the width increases, the Laplacian eigenfunctions evolve, a situation that can be viewed from different perspectives. *Left:* When the width is smaller than the length, the dominant eigenfunction is a vertical sinusoid, but as the width grows, this dominant eigenfunction suddenly becomes a horizontal sinusoid. The kink occurs at the point of multiplicity when width equals length. Similarly, the subdominant eigenfunction suddenly transitions from a horizontal to a vertical orientation. *Right:* An alternative, more useful perspective is that the eigenfunctions do *not* suddenly change and do not have kinks. Rather, their eigenvalues cross over, exchanging dominance. This is the correct mathematical structure. It eliminates fake kinks that do not exist, and that obstruct efficient implementation using neural networks. It supports applications such as transferring data from one shape to another and differentiating eigenanalysis-dependent quantities throughout shape space, including at points of multiplicity.

with an *explicit, continuous dependence on shape parameters*. This focus on shape-dependence allows capturing the evolution of eigenfunctions with shape, enabling applications such as analysis and optimization over shape spaces, predicting eigenfunctions of incomplete shapes, and even computing eigenfunctions in higher dimensions where discrete operators are less explored, and meshing becomes intractable.

Challenges. However, the explicit dependence on shape comes with interesting new challenges. For a single shape, eigenfunctions are typically labeled, computed, and discussed in terms of the order of their dominance, corresponding to a monotonic sequence of eigenvalues. For a shape space, we can no longer think in terms of monotonicity because eigenvalues as functions over shape space often cross and exchange dominance (see Fig. 1-right).

A misguided attempt to cling to monotonicity across the entire shape space (see Fig. 1-left) destroys crucial information about the evolution of eigenfunctions over shape space. As we will show, maintaining the right “topological structure” of eigenfunctions over

shape space as they cross each other is critical to applications such as mapping data from one shape to another or differentiating eigenvalues or eigenfunctions with respect to shape parameters.

On the other hand, dropping reliance on a monotonic sequence of eigenvalues calls into question the very way in which we conduct eigenanalysis. Before we delve into this, let us recap the variational perspective on eigenanalysis for a specific, non-parametric shape.

Peeling off eigenfunctions. Consider the domain Ω with boundary $\partial\Omega$. We eigenanalyze the Laplace operator, $\Delta \equiv \operatorname{div} \operatorname{grad} \equiv \nabla \cdot \nabla$, over Ω using an iterative “peeling” approach, where the i ’th eigenfunction $\phi_i(\mathbf{x}) : \Omega \rightarrow \mathbb{R}$ is discovered after the former, in increasing eigenvalue order.

The first eigenfunction $\phi_1(\mathbf{x})$ minimizes Dirichlet energy

$$E_D[\phi] = \frac{1}{2} \int_{\Omega} |\nabla \phi|^2 d\Omega, \quad (1)$$

among $S = \{f \in L^2(\Omega) \mid \|f\|_2 = 1\}$, the unit-norm square-integrable functions in Ω . (In principle, an eigenfunction need not have a unit norm, but this approach simplifies things.)

Since we have not explicitly enforced any boundary conditions, the minimizer will satisfy the *natural* condition, which for the Dirichlet energy is the *vanishing Neumann* condition, $\frac{\partial \phi_i}{\partial n} = 0$ on $\partial\Omega$.

Let’s get peeling! The second eigenfunction *also* minimizes Dirichlet energy, but this time among ϕ_1^\perp , the *orthogonal complement* to ϕ_1 in S . And so forth. The i ’th eigenfunction minimizes Dirichlet energy among $\operatorname{span}\{\phi_1, \dots, \phi_{i-1}\}^\perp$ orthogonal to earlier modes.

Now that we have the unit-norm eigenfunctions $\{\phi_i\}$, it is straightforward to show that the corresponding eigenvalues are simply their corresponding Dirichlet energies: $\lambda_i = E_D[\phi_i]$, $\lambda_1 \leq \lambda_2 \leq \lambda_3 \dots$

Causality. While the resulting eigenfunctions are mutually orthogonal, the term *mutual* might connote a symmetry that does not, in fact, exist. Peeling is a *sequential process* that produces eigenfunctions in order, seeking minimizers in a descending chain of subspaces. Each subspace is *defined* by what has been found before, establishing a *causal relationship*: the former eigenfunction restricts the solution space for the latter, whereas the latter has no effect on the former. This causal relationship is inherent to the “minimal-energy” view of eigenanalysis and will significantly impact the development of our algorithm.

Shape-dependent eigenfunctions. Inherent to this peeling procedure is the view that we can discover eigenfunctions in increasing order of Dirichlet energy (equivalently: eigenvalue). Alas, would that it were so easy over families of shapes!

For shapes parameterized by one or more design parameters $\mathbf{g} = \{g_i\} \in \mathcal{D} \subset \mathbb{R}^k$, the resulting eigenfunctions and corresponding Dirichlet energies (eigenvalues) are functions over \mathbf{g} . As if to thwart our peeling approach, in general, *it can no longer be true* that $\lambda_1(\mathbf{g}) \leq \lambda_2(\mathbf{g})$ since eigenvalues may exchange dominance as shape evolves (recall Fig. 1).

Can we peel across shape space? An initial, straightforward attempt to generalize peeling might be to modify the domain of integration to include shape space. In this approach, the first eigenfunction $\phi_1(\mathbf{g}, \mathbf{x})$ minimizes the integral of Dirichlet energy over shape space $\int_{\mathcal{D}} E_D[\phi_1(\mathbf{g})] d\mathcal{D}$, the second eigenfunction $\phi_2(\mathbf{g}, \mathbf{x})$

does the same but restricted to ϕ_1^\perp , and so forth. Unfortunately, such *sequential* peeling inherently yields “eigenfunctions” that maintain the same dominance relationship across all of shape space, a false structure (recall Fig. 1-left) that misses all smooth crossovers and replaces them with undesirable kinks, frustrating applications such as transfer of data from one shape to another, inverse design across shape spaces, and so forth.

What is needed is a flexible approach that doesn’t rigidly require consistent dominance relationships across shape space.

A neural fields implementation. We find it most natural to present such a flexible peeling approach in the context of neural field training. Each eigenfunction will be modeled as a separate multilayer perceptron (MLP) mapping shape parameters, $\mathbf{g} \in \mathcal{D}$, and domain position, $\mathbf{x} \in \Omega$, to eigenfunction value, $\phi_i(\mathbf{g}, \mathbf{x})$. Such neural fields are typically trained by overfitting [Mildenhall et al. 2021; Park et al. 2019a] or via a physics-informed neural networks (PINN) approach [Chen et al. 2023a; Raissi et al. 2019; Yang et al. 2021]. Our variational definition of eigenfunctions well-suits the latter view.

Unfortunately, eigenanalysis presents three interwoven challenges: (1) We are interested in finding the multiple eigenfunctions governed by coupled energy minimization principles over a descending chain of spaces. (2) Each minimization problem is restricted to a subspace determined by the solution of all preceding minimizations, inducing a *causal relation*. Finally, (3) the *ordering* of these causal relationships will vary across shape space, so it cannot be determined in advance. These challenges are not present in prior work on PINNs, necessitating changes to standard PINN training.

Dynamically-ordered causality-respecting training. To address these challenges, our novel training method includes three interconnected concepts, all three *strictly required* to obtain eigenfunctions that evolve continuously with shape:

- (1) **Concurrent learning:** As we have seen, sequential peeling produces an incorrect structure because no single ordering of eigenfunctions is valid across all of the shape space. Therefore, we *must* learn n eigenfunctions *concurrently*.
- (2) **Gradient causal filtering:** As we shall see, a naïve approach to concurrent learning suffers from an action-reaction artifact, whereby functions earlier in the causal chain are affected by an orthogonality constraint that should only affect functions subsequent in the chain. To address this, our back-propagation filters the gradient to enforce the causality of the orthogonality constraint.
- (3) **Shape-dependent causal sorting:** Since the ordering of causal relations cannot be predetermined and indeed varies over shape space, we determine the order dynamically. At each evaluation of the loss function, we re-establish the causal ordering of orthogonality constraints based on the relative dominance of eigenvalues.

Necessity of these three advances: These three interwoven concepts are all *required* for our method to achieve, for the first time, a shape-dependent eigenfunction representation that correctly tracks crossovers of eigenvalues at points of multiplicity.

This approach enables learning across families of shapes, facilitating applications such as the prediction of eigenfunctions on incomplete shapes and enabling interactive manipulation across

shape families. We show that our dynamic reordering encourages smoother eigenfunctions across different shapes. Furthermore, our approach transcends the limitations of traditional discrete operators by extending to higher dimensions, where discrete methods are less explored, opening up new avenues for exploration and application.

2 RELATED WORK

2.1 Laplacian Eigenfunctions

Eigenfunctions of Laplace operator have a broad range of applications such as deformation and simulation [Benchekroun et al. 2023; Jacobson et al. 2014], shape matching [Mateus et al. 2008; Ovsjanikov et al. 2012; Sharma and Horaud 2010; Sun et al. 2023], partial shape localization [Rampini et al. 2019], constructing neural networks for geometry learning [Sharp et al. 2022; Smirnov and Solomon 2021], sound analysis [Kac 1966]. They are also known as manifold harmonics because they extended classical spectral harmonics to generalized manifolds [Melzi et al. 2018; Vallet and Lévy 2008].

The most straightforward approach to calculating the eigenfunctions for a given shape is to mesh the domain and perform eigendecomposition on the constructed discrete Laplace-Beltrami operator. Earlier works have discussed the desired properties of the Laplace operator [Wardetzky et al. 2007]. Despite the availability of various methods [Belkin et al. 2008, 2009; Bobenko and Springborn 2005; Fisher et al. 2006; Gueziec et al. 1999; Liu et al. 2017; Sellán et al. 2019; Sharp and Crane 2020; Shimada and Gossard 1995], each with its own advantages, the most commonly adopted discrete operator is the cotangent matrix. After obtaining the Laplace matrix, the eigenvector can be calculated by different eigensolvers [Arbenz et al. 2005; Duersch et al. 2018; Nasikun and Hildebrandt 2022]. However, all these approaches rely on a discrete Laplace operator and perform eigenanalysis on that matrix. Consequently, they are not designed to calculate eigenfunctions across families of shapes.

There are also methods that aim to find corresponding Laplace operators after mesh coarsening [Kyng and Sachdeva 2016; Liu et al. 2019; Nasikun et al. 2018; Öztireli et al. 2010]. Essentially, these methods calculate the corresponding eigenfunctions of the Laplace operator for different discretizations of the same shape. In contrast, our primary goal is to compute eigenfunctions across different shapes. Some prior work in correspondence learning computed other basis functions designed for specific tasks to replace the original Laplace eigenfunctions [Huang et al. 2021; Jiang et al. 2023; Marin et al. 2020a]. We focus on Laplace eigenfunctions due to their wide range of applications. Additionally, there are efforts to recover shapes or perform shape optimization from eigenvalues [Cosmo et al. 2019; Marin et al. 2020b, 2021], while our method finds corresponding eigenfunctions for a given shape family.

2.2 Neural Fields

A neural field [Xie et al. 2021] parameterizes a spatially dependent vector field through a neural network. Early seminal efforts by Chen and Zhang [2019]; Mescheder et al. [2019]; Park et al. [2019b] utilized this framework for encoding signed distance fields, wherein each distinct latent vector represents a unique geometry. Neural fields have since been extensively applied in various domains, including neural rendering [Mildenhall et al. 2020], 3D reconstruction [Wang

et al. 2021; Yariv et al. 2020], geometry processing [Aigerman et al. 2022; Dodik et al. 2023; Mehta et al. 2022; Yang et al. 2021], topology optimization [Zehnder et al. 2021], constitutive modeling [Li et al. 2023], and solving diverse PDE problems [Chang et al. 2023; Chen et al. 2022, 2023b; Deng et al. 2023; Raissi et al. 2019].

As a major point of departure from prior neural field works that use neural networks to parameterize signed distance fields, our work introduces neural fields that parameterize Laplacian Eigenfunctions. Crucially, unlike traditional representations (e.g., mesh and grid), neural fields possess the unique ability to condition on geometric information (e.g., high-dimensional shape latent codes), enabling the computation of Laplacian Eigenfunctions for a large family of shapes. Furthermore, in contrast with prior works that fit neural fields to existing geometric data, our approach trains Eigen neural fields in a geometry-informed fashion *without* any training data.

3 WARM UP: TRAINING OVER ONE SHAPE

We begin by finding the eigenfunctions for a single shape. This exercise will circumnavigate the challenges discussed in the introduction while helping to establish some of the basics of the implementation.

3.1 Overview of Transformations

We seek the first k eigenfunctions $\{\phi_1, \phi_2, \dots, \phi_k\}$, $\phi_i : \Omega \rightarrow \mathbb{R}$. Each ϕ_i is *indirectly* represented by its own MLP, whose weights are trained by minimizing the Dirichlet energy subject to certain constraints. By indirect, we mean that the output $\bar{\phi}_i$ of each MLP undergoes Gram–Schmidt and normalization transformations to produce the eigenfunction ϕ_i :

$$\text{MLP}_i \xrightarrow{\text{inference}} \bar{\phi}_i \xrightarrow{\text{Gram–Schmidt}} \phi_i^p \xrightarrow{\text{normalize}} \phi_i = \arg \min_{\phi} E_D(\phi).$$

3.2 Gram–Schmidt Orthogonalization $\bar{\phi}_i \rightarrow \phi_i^p$

Any two eigenfunctions ϕ_i and ϕ_j , $i \neq j$, must be orthogonal, $\int_{\Omega} \phi_i(x) \phi_j(x) d\Omega = 0$, a constraint we achieve by Gram–Schmidt construction. Given a candidate (unconstrained) function $\bar{\phi}_m$ not yet orthogonal to all previous eigenfunctions, we find its projection ϕ_m^p onto the orthogonal subspace by subtracting from $\bar{\phi}_m$ the component already spanned by the $m-1$ dominating eigenfunctions $\phi = (\phi_1, \dots, \phi_{m-1})$. We seek the λ -weighted linear combination of dominating eigenfunctions ϕ that best approximate $\bar{\phi}_m$,

$$\lambda = \arg \min_{\lambda \in \mathbb{R}^{m-1}} \left\| \lambda^T \phi - \bar{\phi}_m \right\|_2, \quad (2)$$

where $\|\cdot\|_2$ is the Euclidean norm $\|\phi\|_2 = \sqrt{\int_{\Omega} \phi^2 d\Omega}$. Next, we remove the component:

$$\phi_m^p = \bar{\phi}_m - \lambda^T \phi. \quad (3)$$

Integration over Ω is approximated by stochastic cubature, with cubature points drawn from a uniform distribution over Ω .

The gradient $\partial/\partial x \phi_m^p(x)$ is computed, by chain rule, as

$$\frac{\partial \phi_m^p(x)}{\partial x} = \frac{\partial \bar{\phi}_m(x)}{\partial x} - \lambda^T \frac{\partial \phi(x)}{\partial x}. \quad (4)$$

3.3 Normalization $\phi_i^p \rightarrow \phi_i$

We have already successfully constructed a continuous function $\phi^p(\mathbf{x})$ that is orthogonal to previous eigenfunctions. An additional constraint imposed on eigenfunctions is that they maintain a unit norm. While this may seem unnecessary (after all, if ϕ is an eigenfunction, then so is any rescaling $\alpha\phi$), the unit norm constraint achieves two goals: (1) it eliminates the trivial minimizer of Dirichlet energy, the zero function and (2) it equates the Dirichlet energy and the eigenvalue.

We enforce this constraint by normalizing $\phi^p(\mathbf{x})$:

$$\phi(\mathbf{x}) = \frac{\phi^p(\mathbf{x})}{\|\phi^p\|_2}. \quad (5)$$

We accelerate the gradient computation by treating the norm as independent,

$$(\partial/\partial\mathbf{x})\phi \approx \|\phi^p\|_2^{-1}(\partial/\partial\mathbf{x})\phi^p. \quad (6)$$

Now, we have successfully constructed a set of continuous functions that are orthogonal to each other and possess a unit norm.

3.4 Eigenanalysis $\phi_i = \arg \min E_D(\phi)$

What remains is to frame eigenanalysis as an optimization problem. Unit-norm Laplacian eigenfunctions satisfy

$$\Delta\phi(\mathbf{x}) = \lambda\phi(\mathbf{x}) \quad \text{where} \quad \|\phi\|_2 = 1, \quad (7)$$

subject to appropriate conditions over the boundary $\partial\Omega$. Equation 7 is the stationary equation of the corresponding variational problem

$$\min_{\phi \in L^2, \lambda \in \mathbb{R}} E_D[\phi] + \lambda (\|\phi\|_2 - 1). \quad (8)$$

Since ϕ is unit-norm by construction, we need only optimize E_D .

When the variational form of a PDE is minimized without explicitly imposing boundary conditions, *natural* boundary conditions must arise. In our setting, by solely integrating the Dirichlet energy within Ω , we automatically—without imposing boundary conditions—obtain the vanishing Neumann boundary condition

$$\nabla\phi(\mathbf{x}) \cdot \mathbf{n} = 0, \quad \mathbf{x} \in \partial\Omega. \quad (9)$$

Equation 9 holds for all \mathbf{x} on the boundary $\partial\Omega$, where \mathbf{n} denotes the normal vector of the boundary. Figure 14 depicts the results of minimizing E_D using stochastic cubature using a striped shading style that helps to discern boundary behavior.

For SE(3) (or SE(2)) invariance, factoring out the transformations before evaluation can help achieve the corresponding invariance, a common strategy for incorporating invariance in neural networks.

However, even without the factorization, the rotational error appears to be no more significant than the variations caused by re-initializing the network’s weights. Our current eigenfunctions show consistent results under rotational perturbations, as demonstrated in Fig. 15.

3.5 Implementation Notes

Given a uniform sampling $\mathcal{X} = \{\mathbf{x}_1, \dots\}$ over Ω , we optimize the network weights by minimizing

$$\mathcal{L}[\phi_i] = \sum_{\mathbf{x}_j \in \mathcal{X}} \nabla\phi_i(\mathbf{x}_j)^2. \quad (10)$$

ALGORITHM 1: Training on a Single Shape

```

epoch = 0;
repeat
     $\mathbf{x}$  = Sample Domain  $\Omega$ ;
     $\phi_{prev}(\mathbf{x})$  = Ones like  $\mathbf{x}$  ;
        ▷ Hardcode the constant eigenfunction;
    for  $i$  in range  $[0, k)$  do
        Evaluate Network  $\bar{\phi}_i(\mathbf{x})$ ;
        Calculate  $\lambda$  by doing the projection in Equation 2;
        Calculate  $\phi_{m+1}^p(\mathbf{x})$  by Equation 3;
        Calculate  $\phi(\mathbf{x})$  by Equation 5;
        Evaluate gradient  $\frac{\partial\phi(\mathbf{x})}{\partial\mathbf{x}}$  by Equation 4, 6;
        Calculate loss  $\mathcal{L}$  by Equation 10 ;
        Backward loss ;
        Concatenate  $\phi_{prev}(\mathbf{x})$  with  $\phi_i(\mathbf{x})$  and detach;
        ▷ Update for future orthogonal constraints;
    end
    epoch = epoch + 1 ;
until epoch = MaxEpoch;

```

We found that applying positional encoding [Mildenhall et al. 2021], also known as Fourier Features [Tancik et al. 2020], can improve performance.

Algorithm 1 presents a pseudo-code for training on a single shape. Our implementation utilizes PyTorch. The gradient $\nabla\phi_i(\mathbf{x})$ is computed using autodiff, and the least squares projection when calculating $\hat{\mathbf{x}}$ is implemented through PyTorch’s `linalg.solve()`. The first eigenfunction, which (for Neumann boundary conditions) is always the constant function, is hardcoded.

4 TRAINING OVER SHAPE SPACE

Now we dive into training over shape spaces $\{\Omega_g \mid g \in \mathcal{D}\}$ parameterized by geometry code $g \in \mathcal{D}$ drawn from a design space \mathcal{D} . Each eigenfunction $\phi(g, \mathbf{x})$ is now a function of both the geometry code g , and a position $\mathbf{x} \in \Omega_g$.

To obtain the i ’th eigenfunction, we acquire a sample \mathbf{x} from a domain Ω along with its corresponding geometry code g from the shape domain. We then optimize the weights of the network by minimizing the following loss:

We follow the same transformation sequence as before (recall section 3.1). However, this time, we perform cubature over both the geometry code $\mathcal{G} = \{g_i \in \mathcal{D}\}$ and the position $\mathcal{X}_{g_i} = \{\mathbf{x}_j \in \Omega_{g_i}\}$:

$$\mathcal{L} = \sum_{g_i \in \mathcal{G}} \sum_{\mathbf{x}_j \in \mathcal{X}_{g_i}} \nabla_{\mathbf{x}} \phi_i(g_i, \mathbf{x}_j)^2. \quad (11)$$

Observe that the ∇ is only calculating the gradient with respect to \mathbf{x} , discarding the parts related to the geometry code g .

4.1 Gradient Causal Filtering

As previously discussed, the eigenfunctions are differentiated by imposing distinct orthogonal constraints on each eigenfunction. Subsequent eigenfunctions are constructed by projecting out preceding eigenfunctions without influencing them. Eigenfunctions

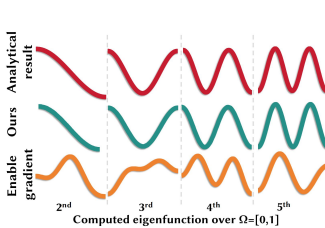
with fewer orthogonal constraints yield lower resulting Dirichlet energy (equivalently: smaller eigenvalues).

It is tempting to enforce causality by training eigenfunctions sequentially: Train the first eigenfunction until convergence, then fix its weights. Train the second, then fix its weights. As we discussed, sequential training produces incorrect results because, in general, no eigenfunction maintains the same causal relationships with its peers over all of the shape space (recall Fig. 1). Therefore, sequential training is not viable, and unfortunately, the simplest way of enforcing causal relationships is not available to us.

The alternative to sequential training is concurrent (parallel) training of the eigenfunctions. This is our only viable path to producing correct results, but as a side bonus, it trains 2 \times to 4 \times faster, too, compared to a sequential approach. In concurrent training, the weights of all eigenfunctions are trained simultaneously. And there lies the rub: since the weights of both the dominating and dominated eigenfunction are free to evolve, the backpropagation of the orthogonality constraint will affect both functions, essentially the “action-reaction” principle of a constraint force.

The incident figure illustrates the action-reaction artifact. Given a dominating function ϕ_1 and a dominated function ϕ_2 subject to the constraint $\phi_2 \in \phi_1^\perp$, there are two ways to decrease the Dirichlet energy of the dominated function, either (1) by making adjustments within the orthogonal subspace ϕ_1^\perp , or (2) by making adjustments to ϕ_1 so as to modify the admissible space ϕ_1^\perp . The first option (“action”) respects causality, whereas the latter (“reaction”) does not; yet both arise from differentiating the constraint $\phi_2 \in \phi_1^\perp$ with respect to ϕ_1 and ϕ_2 .

To eliminate the causality-violating reaction, we must *not* differentiate the constraint with respect to the dominating function. We call this causality-enforcing ignoring of a gradient term **gradient causal filtering**. Such filtering could be used to enforce any causal constraint relationship in parallel training of neural networks, and we use it to protect the causality of the descending chains of orthogonal spaces. We implement the filtering using `detach()` in PyTorch. After detachment, the gradient of the orthogonality constraint is considered *only* with respect to the dominated eigenfunction.



Ablation for gradient filtering. The incident figure compares computations of eigenfunctions over the unit interval, using the full and filtered gradient, compared to the analytic solution (sinusoids satisfying the vanishing Neumann condition). When gradient causal filtering is applied, the resulting eigenfunctions agree with the analytic solution. Without filtering, the result is incorrect.

4.2 Shape-Dependent Causal Sorting

As we discussed in the introduction, fixing the dominance order of the eigenfunctions is undesirable. Recall the example depicted in Fig. 1-left. The trivial, constant eigenfunction ϕ_0 with a zero eigenvalue is not depicted. The green curve depicts the Dirichlet energy minimizer in the subspace $\phi_1 \in \phi_0^\perp$ of E_D . Subsequently, the red curve depicts the Dirichlet energy minimizer in the subspace $\phi_2 \in \phi_1^\perp$. Defining the green and red curves thus leads to two eigenfunction patterns that suddenly swap when the evolving rectangle transitions through a square shape. This swap is undesirable for training and applications. It consumes more network capacity and slows convergence because the spatial field is discontinuous with respect to the geometry code. It leads to artifacts or failures in applications that seek to harness the continuity of eigenfunctions.

Fig. 1-right depicts the desired solution, which has no discontinuity at the square shape. To achieve this solution, we must be aware of the relative eigenvalues (Dirichlet energies) of the two curves at different positions in shape space. For instance, consider an eigenfunction exhibiting a sinusoidal pattern along the horizontal direction (a “horizontally-oriented pattern”). When it has the smallest nonzero eigenvalue, it is the minimizer of E_D in ϕ_0^\perp , i.e., in the subspace orthogonal to the constant function. After the crossover, when it has the second smallest nonzero eigenvalue, it is no longer the minimizer of E_D in ϕ_0^\perp . It is now the minimizer in ϕ_1^\perp , i.e., in the subspace orthogonal to the constant function *and* the vertically-oriented pattern.

The order of projection is determined by the eigenvalue and varies for each shape. Fortunately, for eigenfunctions with a unit norm, the eigenvalue is simply the Dirichlet energy, $\lambda = E_D$. This leads to the algorithm shown in Algorithm 2, where we first evaluate the Dirichlet energy for each unit-norm eigenfunction and then sort to determine the causal ordering for the chain of decreasing subspaces.

With the sorting, we can produce the results shown in Fig. 1-right. As the geometry code evolves, each eigenfunction and eigenvalue evolves smoothly.

5 EVALUATION

In this section, we showcase the accuracy and broad applicability of our method across various settings. We begin by validating our approach using 3D shapes, and then explore its capabilities in higher-dimensional 4D data. Our results highlight diverse applications such as predicting eigenfunctions for incomplete shapes, interactive simulation of reduced order deformables, and gradient-based inverse design. We conclude with an ablation study demonstrating the effectiveness of shape-dependent causal sorting.

5.1 Accuracy of the Method

Evaluation on Shapenet Subset. To validate accuracy, we compare our continuous eigenfunctions with discrete eigenfunctions found by an eigendecomposition of the cotangent Laplacian [Pentland and Williams 1989]. The cotangent Laplacian has been established as convergent to the continuum of the geometry, and its eigenfunctions should therefore provide a reasonable reference under fine geometry.

ALGORITHM 2: Training Over a Shape Space

```

epoch = 0;
repeat
  g = Sample Geometry Code;
  ▷ The geometry code is an explicit shape parameter (e.g., width)
  or a latent variable (e.g., from an auto-decoder).;
  x = Sample Domain Ω;
  Ed = [];
  for i in range [0, k) do
    Evaluate Network  $\bar{\phi}_i(x, g)$  and gradient  $\frac{\partial \bar{\phi}_i(x, g)}{\partial x}$ ;
     $E_d.append(\frac{1}{\sum \bar{\phi}_i(x, g)^2} \sum (\frac{\partial \bar{\phi}_i(x, g)}{\partial x})^2)$ ;
    ▷ Evaluate Dirichlet energy on normalized gradients;
  end
  index, sortedEigenvalue = sort(E_d)
  for idx in range [0, k) do
    i = index[idx]    ▷ Use the order from the sorted index;
    Do projection and optimization same as Algorithm 1;
  end
  epoch = epoch + 1;
until epoch = MaxEpoch;

```

We performed the validation on the ShapeNet dataset, comprised of 50 airplane shapes that we subsequently pre-processed into watertight surfaces Wang et al. [2022], and then tetrahedralized with Tetwild [Hu et al. 2018] to provide a volumetric discretization.

We use these tetrahedralized meshes to construct a cotangent Laplacian matrix, on which we perform an eigendecomposition using the `scipy` library [Virtanen et al. 2020].

As shown in Fig. 4, our resulting solution evaluated at the tetrahedral vertex positions matches the eigenfunctions obtained from the cotangent Laplacian matrix, but importantly our method found these eigenfunctions without requiring any mesh connectivity.

We additionally compare our approach to the eigenfunctions obtained from the Robust-Laplacian [Sharp and Crane 2020], which constructs the Laplacian matrix on point clouds without the need for a meshed topology.

We calculated the first 15 eigenvectors for each of the 50 airplane shapes with both our method and the eigenfunctions of the Robust Laplacian matrix.

We examined the dot product between our method’s eigenfunctions and those obtained from the reference. Since eigenvectors with similar patterns may appear in different orders, we matched each predicted eigenvector (from both our method and Robust-Laplacian) with that counterpart in the ground truth that maximized the inner product. Our method’s average dot product is 0.917, similar to the 0.906 achieved by Robust-Laplacian. Fig. 4 depicts examples of our predicted eigenfunctions alongside the reference. This data suggests that the accuracy of our method is comparable to previous methods that construct explicit Laplacians from a point cloud and then perform standard eigendecomposition.

It is worth noting that while sharing similar accuracies, our method enjoys features that the reference and Robust-Laplacian do not, such as differentiability with respect to shape code, which allows us to perform shape optimization.

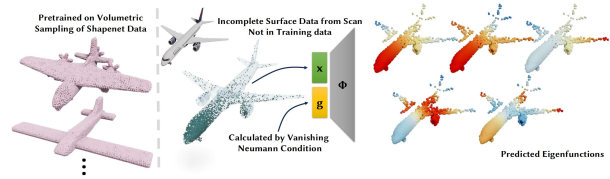


Fig. 2. *Laplacian Eigenfunctions across shapes*. Left: We train the eigenfunctions across various airplane shapes from the shapenet [Chang et al. 2015]. Right: After training, our method is able to predict the eigenfunctions of new shapes from incomplete surface data.

5.2 Computing Eigenmodes for 4D Data

One advantage of our method is its independence from discretization, allowing for generalization to higher dimensions where meshing can easily become intractable and discrete operators are less explored.

We first applied our method to a 4D cube with the unit norm, where we already knew the expected solutions. As depicted in Figure 5, we visualized the non-constant eigenfunctions predicted by our method, omitting the first eigenfunction (the constant function) for simplicity. We know that the first four non-constant eigenfunctions should be sinusoidal functions along each axis. The 1st, 3rd, and 4th non-constant eigenfunctions exhibit sinusoidal changes along the axes of the first three dimensions. The second row displays sinusoidal functions along the 4th dimension: each column indicates that the first three dimensions remain constant while varying along the 4th dimension.

We can further apply our method to more advanced scenarios. We can generate intriguing 4D shapes by interpolating between shapes, where the interpolation between 3D shapes forms the 4th dimension. In Figure 10, we trained a neural SDF with a latent code t . At $t = 0$, the SDF represents a duck, while at $t = 1$, it represents Spot the cow. During inference, the dimension of the latent code can be seen as the fourth dimension, allowing us to query any point between $t = 0$ and $t = 1$. Hence, we can compute the eigenfunctions on this 4D SDF. As depicted in Figure 10, we have displayed the first 10 non-constant eigenfunctions, revealing smoothly changing eigenfunctions along each axis.

5.3 Eigenfunctions Across Various Shapes

Predict Eigenfunctions for Incomplete Shapes. In Figure 2, we illustrate the training of eigenfunctions across a shape space parameterized by a 3-dimensional latent shape code g .

To build the shape space, we source 158 *volumetric* shapes from ShapeNet [Chang et al. 2015], and use an auto-decoder pipeline inspired by Park et al. [2019a] to train a shape decoder. In lieu of an encoder, each training shape is represented by an unknown 3-dimensional latent geometry code g . Post-training, these latent geometry codes are discarded, leaving only the decoder for the continuous 3-dimensional space of volumetric shapes. Finally, we train the volumetric eigenfunctions across this shape space.

As a challenging test case, during inference, we utilize partial scan data, encompassing not *volumetric* but rather *surface* coordinates $x \in \mathcal{S}$ alongside their *surface normals* n .

Since we know that our eigenfunctions have vanishing Neumann conditions at the shape boundary $\partial\Omega$, as shown in Equation 9, we can use the alignment between the surface normals in the query and the pretrained eigenfunction gradients to find the geometry code \mathbf{g} that best fits the query shape:

$$\arg \min_{\mathbf{g}} = \sum_{i=1 \dots k} \sum_{\mathbf{x} \in S} (\nabla \phi_i(\mathbf{g}, \mathbf{x}) \cdot \mathbf{n})^2. \quad (12)$$

We optimize Equation 12 using gradient descent with random initialization of \mathbf{g} . To mitigate the influence of local minima, we employed 30 different random initializations from a normal distribution. The final result is determined by selecting the geometry code with the lowest energy. We use the optimal \mathbf{g} to infer the eigenfunction over the novel, partial scan data.

As illustrated in Figure 2 and Figure 6, the predicted eigenfunctions effectively generate representations corresponding to a complete shape despite the input scan data being incomplete and containing discontinuities on one side of the wing. This is because our eigenfunctions were trained over a shape space that spans only complete shapes.

Interactive Manipulation. Our method also facilitates real-time shape morphing within a family of geometries during reduced-space simulation. As proposed in [Benchekroun et al. 2023], the eigenfunctions for the Laplace operator can serve as the skinning eigenmodes for co-rotational elastic energy. Therefore, we can utilize our eigenfunctions as the skinning eigenmodes to enable seamless shape changes during simulation.

As depicted in Figure 7, we consider a space of chairs parameterized by support radius r ; seatback height h and seatback depth d . By uniformly sampling the geometry code (r, h, d) within the range of $[0.1, 0.4]$, $[0.2, 0.8]$, and $[-0.2, 0.3]$, and training for 150,000 epochs, we obtained a model capable of evaluating eigenfunctions for any shapes falling within the range of the training sampling. As shown in Figure 11, leveraging the efficiency of our method’s network inference, we can recalculate the eigenfunctions at interactive rates when modifying the shape code.

Interactive Inverse Design. Furthermore, the eigenfunctions trained on the chair shape space are *differentiable* with respect to the shape code. We leverage this differentiability, in the spirit of *differential manipulation* [Gleicher and Witkin 1991] and *sensitivity analysis* [Umetani et al. 2011], to automatically design the chair’s shape with respect to the designer’s specified goals. After the designer selects a point in space, the user interface displays a slider with the value of the eigenfunction at the selected point. As shown in Figure 13, the designer may then adjust the slider to a new preferred value for the eigenfunction, and the system will automatically adjust the shape of the chair to achieve the preferred value. Our inverse design framework leverages the ability to differentiate the eigenfunction with respect to the shape code.

5.4 Effectiveness of the Shape-Dependent Causal Sorting

Quantitative Evaluation. To further demonstrate the efficacy of the Shape-Dependent Causal Sorting, we conducted additional evaluations. Our Shape-Dependent Causal Sorting encourages the network to learn smoother eigenfunctions relative to the geometry

code. To quantitatively assess smoothness, we computed the L^2 norm of the gradient with respect to the **geometry code**, denoted as $|\frac{\partial \phi(\mathbf{x}, \mathbf{g})}{\partial \mathbf{g}}|^2$. This can be interpreted as the Dirichlet energy within the **shape space**. We sampled 1,000 geometry codes uniformly within the training range and calculated the average L^2 norm of the gradient. We evaluated this on two families of shapes shown in Figure 7 and Figure 12.

For the example in Figure 7, without sorting, the average norm is 929.61, which is 1.42 times larger than the sorted results at 652.20. For the example in Figure 12, without sorting, the average norm is 385.64, which is 2.05 times larger than the sorted results at 188.18. This discrepancy arises because the fixed order compels the network to change patterns across different shapes, leading to increased irregularity with respect to geometry.

We have also incorporated graphical representations that illustrate the relationship between eigenvalues and varying geometry codes, providing an intuitive demonstration of the impact of sorting. Figure 9 demonstrated the eigenvalues with respect to changing geometry codes.

Ablation Study: Consistency in Data Transfer Across Shapes. Our method better preserves the evolution of eigenfunctions across shapes, demonstrating improved consistency in data transfer across shapes within a family.

To demonstrate this, we first project a target function onto the first 10 eigenfunctions of a shape. This yields a coefficient for each function, and the reconstructed function is obtained by summing the first 10 eigenfunctions weighted by their respective coefficients. We then maintain the coefficients unchanged and evolve the shape code (which also implies changing the eigenfunctions, but the weights for each eigenfunction remain unchanged). Subsequently, we can plot the reconstructed function on the new shape, leveraging the evolution of the eigenfunctions.

As depicted in Figure 8 and Figure 12, the absence of Shape-Dependent Causal Sorting leads to significant changes in the reconstructed function as the shape evolves. This behavior is attributed to undesirable kinks at the crossover points, where the eigenfunctions abruptly change. Such changes disrupt the smooth evolution of eigenfunctions across shapes, resulting in the poor preservation of initial information as the shape evolves.

In contrast, our formulation allows for crossovers, thereby better encouraging a smooth evolution of eigenfunctions. As shown in the second row, with sorting, we are able to better preserve the data transfer as the shape evolves.

6 DISCUSSION AND FUTURE WORK

With these promising results, there remain areas for improvement and expansion. One limitation is the maximum number of eigenfunctions our approach can effectively compute. As the number of eigenfunctions increases, so does their spatial frequency. Accurately training higher frequencies is a known challenge for neural fields.

Compared to standard methods such as eigendecomposition of the Cotan matrix, our training process is slower, and the proposed method is non-competitive for single shapes represented by a triangle mesh, where traditional FEM approaches reign supreme.

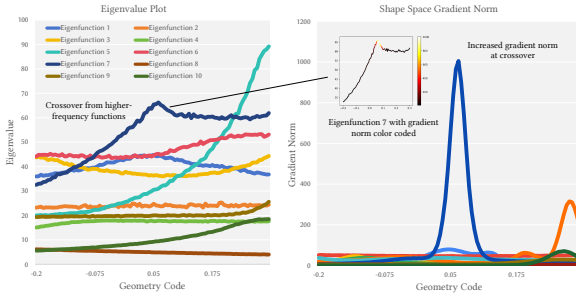


Fig. 3. *Gradient Indicators of Higher-Frequency Crossovers.* The norm of shape space gradients (the gradient with respect to the geometry code $|\frac{\partial\phi(x,g)}{\partial g}|^2$) shows a significant increase at the crossover, therefore can be used as an indicator of the crossover from higher-frequency eigenfunctions.

We have currently limited our scope to Neumann boundary conditions. Eigenfunctions subject to Dirichlet or Robin boundary conditions could be handled in the future by using PINN techniques for enforcing essential boundary conditions, e.g., additional penalization terms that contribute to the loss function [Berrone et al. 2023].

Our implementation of stochastic cubature presently gives uniform weight to all samples. This is appropriate if the cubature is drawn from a uniform distribution. However, certain domain shapes may benefit from nonuniform cubature, such as importance sampling. Additionally, if the shape space spans domains of varying sizes, the number of samples per shape may differ, potentially biasing the training to focus on some regions of shape space over others. Developing cubature rules tailored to the specific domain shapes and/or normalizing the cubature per shape to ensure equal attention across shapes would be valuable directions for future work.

Truncating an infinite-dimensional space with a finite number of subspaces inherently leads to missing information. In our case, this limitation can result in crossovers from higher-frequency eigenfunctions that cannot be fully captured due to the finite number of eigenfunctions used. However, we can identify these problematic functions by evaluating shape space gradients (the gradient with respect to the geometry code $|\frac{\partial\phi(x,g)}{\partial g}|^2$). As shown in Figure 3, there is a significant increase in the gradient norm at points where there is a crossover from a higher-frequency eigenfunction, which serves as a reliable indicator of these crossovers.

Another interesting direction for future work is to make more use of the gradients with respect to the geometry code $\frac{\partial\phi(x,g)}{\partial g}$. By adding penalizing terms on g , we can achieve even smoother evolving functions among shape families.

Despite some limitations, shape-dependent representations of eigenfunctions appear to be a promising and versatile tool for working with eigenfunctions in continuously-parameterized shape spaces.

REFERENCES

Noam Aigerman, Kunal Gupta, Vladimir G Kim, Siddhartha Chaudhuri, Jun Saito, and Thibault Groueix. 2022. Neural Jacobian Fields: Learning Intrinsic Mappings of

Arbitrary Meshes. *arXiv preprint arXiv:2205.02904* (2022).

Peter Arbenz, Ulrich L. Hetmaniuk, Richard B. Lehoucq, and Raymond S. Tuminaro. 2005. A comparison of eigensolvers for large-scale 3D modal analysis using AMG-preconditioned iterative methods. *Internat. J. Numer. Methods Engrg.* 64, 2 (2005), 204–236. <https://doi.org/10.1002/nme.1365> arXiv:<https://onlinelibrary.wiley.com/doi/pdf/10.1002/nme.1365>

Mikhail Belkin, Jian Sun, and Yusu Wang. 2008. Discrete laplace operator on meshed surfaces. In *Proceedings of the Twenty-Fourth Annual Symposium on Computational Geometry* (College Park, MD, USA) (SCG '08). Association for Computing Machinery, New York, NY, USA, 278–287. <https://doi.org/10.1145/1377676.1377725>

Mikhail Belkin, Jian Sun, and Yusu Wang. 2009. Constructing Laplace operator from point clouds in \mathbb{R}^d . In *Proceedings of the Twentieth Annual ACM-SIAM Symposium on Discrete Algorithms* (New York, New York) (SODA '09). Society for Industrial and Applied Mathematics, USA, 1031–1040.

Otman Benchekroun, Jiayi Erie Zhang, Siddhartha Chaudhuri, Eitan Grinspun, Yi Zhou, and Alec Jacobson. 2023. Fast Complementary Dynamics via Skinning Eigenmodes. *ACM Trans. Graph.* 42, 4, Article 106 (jul 2023), 21 pages. <https://doi.org/10.1145/3592404>

S. Berrone, C. Canuto, M. Pintore, and N. Sukumar. 2023. Enforcing Dirichlet boundary conditions in physics-informed neural networks and variational physics-informed neural networks. *Heliyon* 9, 8 (2023), e18820. <https://doi.org/10.1016/j.heliyon.2023.e18820>

Alexander I. Bobenko and Boris A. Springborn. 2005. A Discrete Laplace–Beltrami Operator for Simplicial Surfaces. *Discrete & Computational Geometry* 38 (2005), 740–756. <https://api.semanticscholar.org/CorpusID:708910>

Angel X. Chang, Thomas Funkhouser, Leonidas Guibas, Pat Hanrahan, Qixing Huang, Zimo Li, Silvio Savarese, Manolis Savva, Shuran Song, Hao Su, Jianxiong Xiao, Li Yi, and Fisher Yu. 2015. *ShapeNet: An Information-Rich 3D Model Repository*. Technical Report arXiv:1512.03012 [cs.GR]. Stanford University – Princeton University – Toyota Technological Institute at Chicago.

Yue Chang, Peter Yichen Chen, Zhecheng Wang, Maurizio M. Chiaramonte, Kevin Carlberg, and Eitan Grinspun. 2023. LiCROM: Linear-Subspace Continuous Reduced Order Modeling with Neural Fields. In *SIGGRAPH Asia 2023 Conference Papers* (, Sydney, NSW, Australia) (SA '23). Association for Computing Machinery, New York, NY, USA, Article 111, 12 pages. <https://doi.org/10.1145/3610548.3618158>

Honglin Chen, Rundi Wu, Eitan Grinspun, Changxi Zheng, and Peter Yichen Chen. 2022. Implicit Neural Spatial Representations for Time-dependent PDEs. *arXiv preprint arXiv:2210.00124* (2022).

Honglin Chen, Rundi Wu, Eitan Grinspun, Changxi Zheng, and Peter Yichen Chen. 2023a. Implicit Neural Spatial Representations for Time-dependent PDEs. In *International Conference on Machine Learning*.

Peter Yichen Chen, Jinxu Xiang, Dong Heon Cho, Yue Chang, G A Pershing, Henrique Teles Maia, Maurizio M Chiaramonte, Kevin Thomas Carlberg, and Eitan Grinspun. 2023b. CROM: Continuous Reduced-Order Modeling of PDEs Using Implicit Neural Representations. In *The Eleventh International Conference on Learning Representations*. <https://openreview.net/forum?id=FUORz1tG8Og>

Zhiqin Chen and Hao Zhang. 2019. Learning implicit fields for generative shape modeling. In *Proceedings of the IEEE/CVF Conference on Computer Vision and Pattern Recognition*. 5939–5948.

Luca Cosmo, Mikhail Panine, Arianna Rampini, Maks Ovsjanikov, Michael M. Bronstein, and Emanuele Rodola. 2019. Isospectralization, or How to Hear Shape, Style, and Correspondence. In *The IEEE Conference on Computer Vision and Pattern Recognition (CVPR)*.

Yitong Deng, Hong-Xing Yu, Diyang Zhang, Jiajun Wu, and Bo Zhu. 2023. Fluid Simulation on Neural Flow Maps. *ACM Trans. Graph.* 42, 6, Article 248 (2023).

Ana Dodik, Oded Stein, Vincent Sitzmann, and Justin Solomon. 2023. Variational Barycentric Coordinates. *ACM Transactions on Graphics* (2023). <https://doi.org/10.1145/3618403>

Jed A. Duersch, Meiyue Shao, Chao Yang, and Ming Gu. 2018. A Robust and Efficient Implementation of LOBPCG. *SIAM Journal on Scientific Computing* 40, 5 (2018), C655–C676. <https://doi.org/10.1137/17M1129830> arXiv:<https://doi.org/10.1137/17M1129830>

Matthew Fisher, Boris Springborn, Alexander I. Bobenko, and Peter Schroder. 2006. An algorithm for the construction of intrinsic delaunay triangulations with applications to digital geometry processing. In *ACM SIGGRAPH 2006 Courses* (Boston, Massachusetts) (SIGGRAPH '06). Association for Computing Machinery, New York, NY, USA, 69–74. <https://doi.org/10.1145/1185657.1185668>

Michael Gleicher and Andrew P. Witkin. 1991. Differential Manipulation *. <https://api.semanticscholar.org/CorpusID:1257589>

A. Gueziec, F. Bossen, G. Taubin, and C. Silva. 1999. Efficient compression of non-manifold polygonal meshes. In *Proceedings Visualization '99 (Cat. No.99CB37067)*. 73–512. <https://doi.org/10.1109/VISUAL.1999.809870>

Yixin Hu, Qingnan Zhou, Xifeng Gao, Alec Jacobson, Denis Zorin, and Daniele Panozzo. 2018. Tetrahedral Meshing in the Wild. *ACM Trans. Graph.* 37, 4, Article 60 (July 2018), 14 pages. <https://doi.org/10.1145/3197517.3201353>

Jiahui Huang, Tolga Birdal, Zan Gojcic, Leonidas J Guibas, and Shi-Min Hu. 2021. Multiway Non-rigid Point Cloud Registration via Learned Functional Map Synchronization. *arXiv preprint arXiv:2111.12878* (2021).

Alec Jacobson, Zhigang Deng, Ladislav Kavan, and JP Lewis. 2014. Skinning: Real-time Shape Deformation. In *ACM SIGGRAPH 2014 Courses*.

Puhua Jiang, Mingze Sun, and Ruqi Huang. 2023. Neural Intrinsic Embedding for Non-rigid Point Cloud Matching. In *Proceedings of the IEEE/CVF Conference on Computer Vision and Pattern Recognition*. 21835–21845.

Mark Kac. 1966. Can One Hear the Shape of a Drum? *The American Mathematical Monthly* 73, 4 (1966), 1–23. <http://www.jstor.org/stable/2313748>

Rasmus Kyng and Sushant Sachdeva. 2016. Approximate Gaussian Elimination for Laplacians - Fast, Sparse, and Simple. In *2016 IEEE 57th Annual Symposium on Foundations of Computer Science (FOCS)*. 573–582. <https://doi.org/10.1109/FOCS.2016.68>

Yue Li, Stelian Coros, and Bernhard Thomaszewski. 2023. Neural Metamaterial Networks for Nonlinear Material Design. *ACM Transactions on Graphics (TOG)* 42, 6 (2023), 1–13.

Hsueh-Ti Derek Liu, Alec Jacobson, and Maks Ovsjanikov. 2019. Spectral coarsening of geometric operators. *ACM Trans. Graph.* 38, 4, Article 105 (jul 2019), 13 pages. <https://doi.org/10.1145/3306346.3322953>

Yong-Jin Liu, Dian Fan, Chun-Xu Xu, and Ying He. 2017. Constructing Intrinsic Delaunay Triangulations from the Dual of Geodesic Voronoi Diagrams. *ACM Trans. Graph.* 36, 2, Article 15 (apr 2017), 15 pages. <https://doi.org/10.1145/2999532>

Riccardo Marin, Marie-Julie Rakotosaona, Simone Melzi, and Maks Ovsjanikov. 2020a. Correspondence learning via linearly-invariant embedding. *Advances in Neural Information Processing Systems* 33 (2020).

Riccardo Marin, Arianna Rampini, Umberto Castellani, Emanuele Rodola, Maks Ovsjanikov, and Simone Melzi. 2020b. Instant recovery of shape from spectrum via latent space connections. In *2020 International Conference on 3D Vision (3DV)*. IEEE, 120–129.

Riccardo Marin, Arianna Rampini, Umberto Castellani, Emanuele Rodola, Maks Ovsjanikov, and Simone Melzi. 2021. Spectral Shape Recovery and Analysis Via Data-driven Connections. *International Journal of Computer Vision* (2021), 1–16.

Diana Mateus, Radu Horaud, David Knossow, Fabio Cuzzolin, and Edmond Boyer. 2008. Articulated shape matching using Laplacian eigenfunctions and unsupervised point registration. In *2008 IEEE Conference on Computer Vision and Pattern Recognition*. 1–8. <https://doi.org/10.1109/CVPR.2008.4587538>

Ishit Mehta, Manmohan Chandraker, and Ravi Ramamoorthi. 2022. A level set theory for neural implicit evolution under explicit flows. In *Computer Vision–ECCV 2022: 17th European Conference, Tel Aviv, Israel, October 23–27, 2022, Proceedings, Part II*. Springer, 711–729.

S. Melzi, E. Rodola, U. Castellani, and M. M. Bronstein. 2018. Localized Manifold Harmonics for Spectral Shape Analysis. *Computer Graphics Forum* 37, 6 (2018), 20–34. <https://doi.org/10.1111/cgf.13309> arXiv:<https://onlinelibrary.wiley.com/doi/pdf/10.1111/cgf.13309>

Lars Mescheder, Michael Oechsle, Michael Niemeyer, Sebastian Nowozin, and Andreas Geiger. 2019. Occupancy networks: Learning 3d reconstruction in function space. In *Proceedings of the IEEE/CVF Conference on Computer Vision and Pattern Recognition*. 4460–4470.

Ben Mildenhall, Pratul P Srinivasan, Matthew Tancik, Jonathan T Barron, Ravi Ramamoorthi, and Ren Ng. 2020. Nerf: Representing scenes as neural radiance fields for view synthesis. In *European conference on computer vision*. Springer, 405–421.

Ben Mildenhall, Pratul P. Srinivasan, Matthew Tancik, Jonathan T. Barron, Ravi Ramamoorthi, and Ren Ng. 2021. NeRF: representing scenes as neural radiance fields for view synthesis. *Commun. ACM* 65, 1 (dec 2021), 99–106. <https://doi.org/10.1145/3503250>

Ahmad Nasikun, Christopher Brandt, and Klaus Hildebrandt. 2018. Fast Approximation of Laplace-Beltrami Eigenproblems. *Computer Graphics Forum* 37, 5 (2018), 121–134. <https://doi.org/10.1111/cgf.13496> arXiv:<https://onlinelibrary.wiley.com/doi/pdf/10.1111/cgf.13496>

Ahmad Nasikun and Klaus Hildebrandt. 2022. The Hierarchical Subspace Iteration Method for Laplace-Beltrami Eigenproblems. *ACM Trans. Graph.* 41, 2, Article 17 (jan 2022), 14 pages. <https://doi.org/10.1145/3495208>

Maks Ovsjanikov, Mirela Ben-Chen, Justin Solomon, Adrià Butscher, and Leonidas Guibas. 2012. Functional maps: a flexible representation of maps between shapes. *ACM Trans. Graph.* 31, 4, Article 30 (jul 2012), 11 pages. <https://doi.org/10.1145/2185520.2185526>

A. Cengiz Özfireli, Marc Alexa, and Markus Gross. 2010. Spectral sampling of manifolds. *ACM Trans. Graph.* 29, 6, Article 168 (dec 2010), 8 pages. <https://doi.org/10.1145/1882261.1866190>

Jeong Joon Park, Peter Florence, Julian Straub, Richard Newcombe, and Steven Lovegrove. 2019a. DeepSDF: Learning Continuous Signed Distance Functions for Shape Representation. In *The IEEE Conference on Computer Vision and Pattern Recognition (CVPR)*.

Jeong Joon Park, Peter Florence, Julian Straub, Richard Newcombe, and Steven Lovegrove. 2019b. DeepSDF: Learning continuous signed distance functions for shape representation. In *Proceedings of the IEEE/CVF Conference on Computer Vision and Pattern Recognition*. 165–174.

A. Pentland and J. Williams. 1989. Good vibrations: modal dynamics for graphics and animation. In *Proceedings of the 16th Annual Conference on Computer Graphics and Interactive Techniques (SIGGRAPH '89)*. Association for Computing Machinery, New York, NY, USA, 215–222. <https://doi.org/10.1145/74333.74355>

Maziar Raissi, Paris Perdikaris, and George E Karniadakis. 2019. Physics-informed neural networks: A deep learning framework for solving forward and inverse problems involving nonlinear partial differential equations. *J. Comput. Phys.* 378 (2019), 686–707.

Arianna Rampini, Irene Tallini, Maks Ovsjanikov, Alexander M. Bronstein, and Emanuele Rodolà. 2019. Correspondence-Free Region Localization for Partial Shape Similarity via Hamiltonian Spectrum Alignment. *CoRR* abs/1906.06226 (2019). arXiv:1906.06226 <http://arxiv.org/abs/1906.06226>

Silvia Sellan, Hering Yi Cheng, Yuming Ma, Mitchell Dembowski, and Alec Jacobson. 2019. Solid Geometry Processing on Deconstructed Domains. *Computer Graphics Forum* (2019). <https://doi.org/10.1111/cgf.13592>

Avinash Sharma and Radu Horaud. 2010. Shape matching based on diffusion embedding and on mutual isometric consistency. In *2010 IEEE Computer Society Conference on Computer Vision and Pattern Recognition - Workshops*. 29–36. <https://doi.org/10.1109/CVPRW.2010.5543278>

Nicholas Sharp, Souhaib Attaiki, Keenan Crane, and Maks Ovsjanikov. 2022. Diffusion-Net: Discretization Agnostic Learning on Surfaces. *ACM Trans. Graph.* 41, 3, Article 27 (mar 2022), 16 pages. <https://doi.org/10.1145/3507905>

Nicholas Sharp and Keenan Crane. 2020. A Laplacian for Nonmanifold Triangle Meshes. *Computer Graphics Forum (SGP)* 39, 5 (2020).

Kenji Shimada and David C. Gossard. 1995. Bubble mesh: automated triangular meshing of non-manifold geometry by sphere packing. In *Proceedings of the Third ACM Symposium on Solid Modeling and Applications* (Salt Lake City, Utah, USA) (SMA '95). Association for Computing Machinery, New York, NY, USA, 409–419. <https://doi.org/10.1145/218013.218095>

Dmitry Smirnov and Justin Solomon. 2021. HodgeNet: Learning Spectral Geometry on Triangle Meshes. *SIGGRAPH* (2021).

Mingze Sun, Shiwei Mao, Puhua Jiang, Maks Ovsjanikov, and Ruqi Huang. 2023. Spatially and Spectrally Consistent Deep Functional Maps. In *2023 IEEE/CVF International Conference on Computer Vision (ICCV)*. 14451–14461. <https://doi.org/10.1109/ICCV51070.2023.01333>

Matthew Tancik, Pratul P. Srinivasan, Ben Mildenhall, Sara Fridovich-Keil, Nithin Raghavan, Utkarsh Singhal, Ravi Ramamoorthi, Jonathan T. Barron, and Ren Ng. 2020. Fourier features let networks learn high frequency functions in low dimensional domains. In *Proceedings of the 34th International Conference on Neural Information Processing Systems* (, Vancouver, BC, Canada.) (NIPS '20). Curran Associates Inc., Red Hook, NY, USA, Article 632, 11 pages.

Nobuyuki Umetani, Danny M. Kaufman, Takeo Igarashi, and Eitan Grinspun. 2011. Sensitive couture for interactive garment modeling and editing. *ACM Trans. Graph.* 30, 4, Article 90 (jul 2011), 12 pages. <https://doi.org/10.1145/2010324.1964985>

B. Vallet and B. Lévy. 2008. Spectral Geometry Processing with Manifold Harmonics. *Computer Graphics Forum* 27, 2 (2008), 251–260. <https://doi.org/10.1111/j.1467-8659.2008.01122.x> arXiv:<https://onlinelibrary.wiley.com/doi/pdf/10.1111/j.1467-8659.2008.01122.x>

Pauli Virtanen, Ralf Gommers, Travis E. Oliphant, Matt Haberland, Tyler Reddy, David Cournapeau, Evgeni Burovski, Pearu Peterson, Warren Weckesser, Jonathan Bright, Stéfan J. van der Walt, Matthew Brett, Joshua Wilson, K. Jarrod Millman, Nikolay Mayorov, Andrew R. J. Nelson, Eric Jones, Robert Kern, Eric Larson, C. J. Carey, İlhan Polat, Yu Feng, Eric W. Moore, Jake VanderPlas, Denis Laxalde, Josef Perktold, Robert Cimrman, Ian Henriksen, E. A. Quintero, Charles R. Harris, Anne M. Archibald, António H. Ribeiro, Fabian Pedregosa, Paul van Mulbregt, and SciPy 1.0 Contributors. 2020. SciPy 1.0: Fundamental Algorithms for Scientific Computing in Python. *Nature Methods* 17 (2020), 261–272. <https://doi.org/10.1038/s41592-019-0686-2>

Peng Wang, Lingjie Liu, Yuan Liu, Christian Theobalt, Taku Komura, and Wenping Wang. 2021. NeuS: Learning Neural Implicit Surfaces by Volume Rendering for Multi-view Reconstruction. *Advances in Neural Information Processing Systems* 34 (2021), 27171–27183.

Peng-Shuai Wang, Yang Liu, and Xin Tong. 2022. Dual Octree Graph Networks for Learning Adaptive Volumetric Shape Representations. *ACM Transactions on Graphics (SIGGRAPH)* 41, 4 (2022).

Max Wardetzky, Saurabh Mathur, Felix Kälberer, and Eitan Grinspun. 2007. Discrete laplace operators: no free lunch. In *Proceedings of the Fifth Eurographics Symposium on Geometry Processing (<conf-loc>, <city>Barcelona</city>, <country>Spain</country>, </conf-loc>)* (SGP '07). Eurographics Association, Goslar, DEU, 33–37.

Yiheng Xie, Towaki Takikawa, Shunsuke Saito, Or Litany, Shiqin Yan, Numair Khan, Federico Tombari, James Tompkin, Vincent Sitzmann, and Srinath Sridhar. 2021. Neural Fields in Visual Computing and Beyond. *arXiv preprint arXiv:2111.11426* (2021).

Guandao Yang, Serge Belongie, Bharath Hariharan, and Vladlen Koltun. 2021. Geometry Processing with Neural Fields. In *Thirty-Fifth Conference on Neural Information Processing Systems*.

Lior Yariv, Yoni Kasten, Dror Moran, Meirav Galun, Matan Atzmon, Basri Ronen, and Yaron Lipman. 2020. Multiview neural surface reconstruction by disentangling geometry and appearance. *Advances in Neural Information Processing Systems* 33 (2020), 2492–2502.

Jonas Zehnder, Yue Li, Stelian Coros, and Bernhard Thomaszewski. 2021. Ntopo: Mesh-free topology optimization using implicit neural representations. *Advances in Neural Information Processing Systems* 34 (2021), 10368–10381.

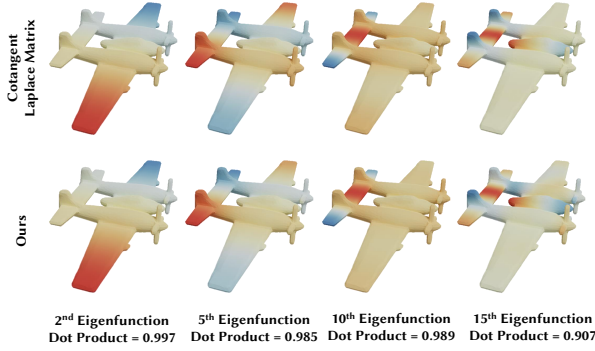


Fig. 4. Comparison with eigenfunctions from cotangent Laplacians. The eigenfunctions obtained using our method are compared with those derived from a Cotangent Laplace Matrix. The accuracy of our approach is comparable to that of previous methods that construct matrices from point cloud sampling.

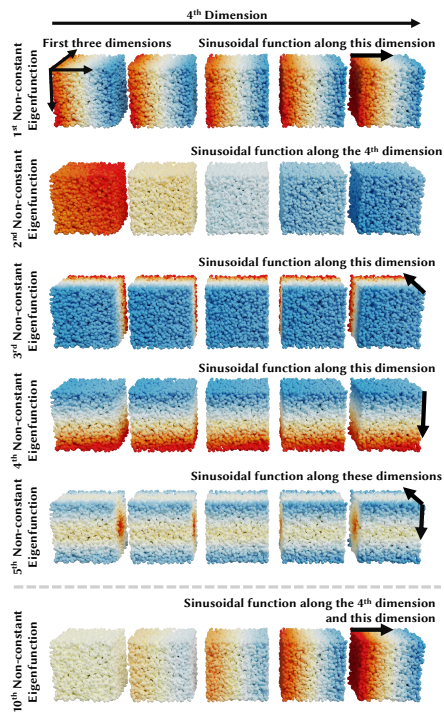


Fig. 5. Eigenfunctions of a 4D Cube. We visualized the non-constant eigenfunctions predicted by our method on a 4D cube. The first four non-constant eigenfunctions accurately capture the sinusoidal function along each of the four dimensions. We observe a mean squared error (MSE) of 1×10^{-4} to 5×10^{-4} over all eigenfunctions compared with analytical solutions.

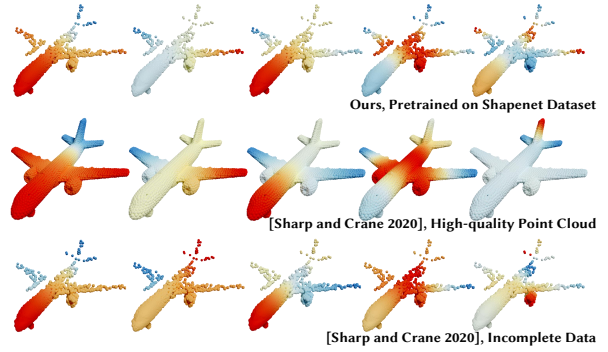


Fig. 6. Shapenet. Our method, pre-trained on ShapeNet, can predict the eigenfunction of an entire shape from an incomplete surface scan. We compared our results with those obtained by applying the method from [Sharp and Crane 2020] to a high-quality sampling of the original shape, as well as directly applying [Sharp and Crane 2020] results in discontinuities in the eigenfunction where the sampling is incomplete, whereas our method shows fewer discontinuities in those areas.

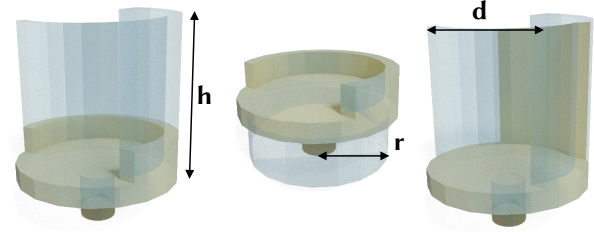


Fig. 7. Illustration of manually designed shape code. We designed a space of chairs parameterized by support radius r ; seatback height h and seatback depth d .

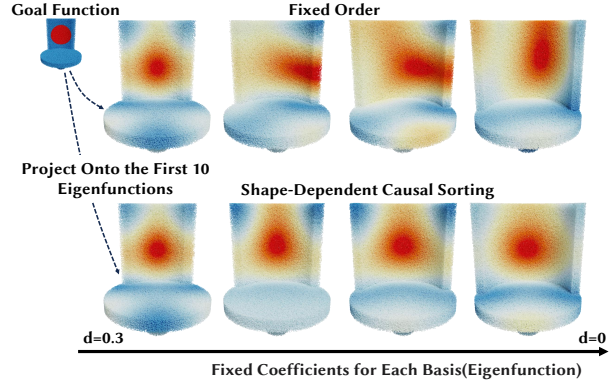


Fig. 8. Information Transfer. Our method better preserves the evolution of eigenfunctions across shapes, demonstrating improved consistency in data transfer across shapes within a family.

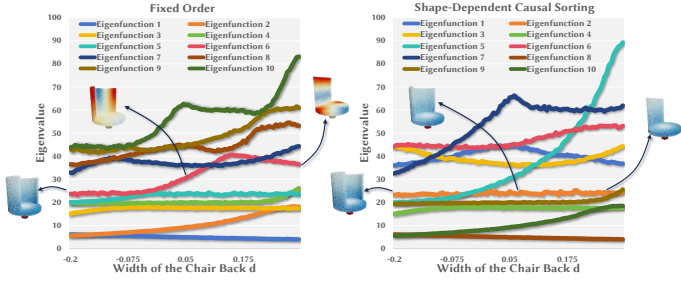


Fig. 9. *Eigenvalue Crossover*. We calculated the eigenvalue for each function for fixed $r = 0.1$ and $h = 0.8$, with varying d . The left part shows the results in a fixed order, while the right part shows the results with Shape-dependent causal sorting.

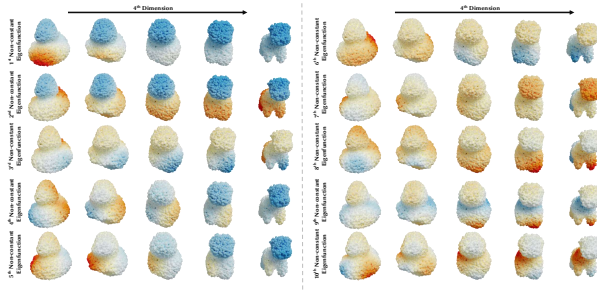


Fig. 10. *4D Example: shape interpolation*. We can apply our method to calculate the eigenfunctions for shape interpolation by treating the interpolation as a 4D shape.

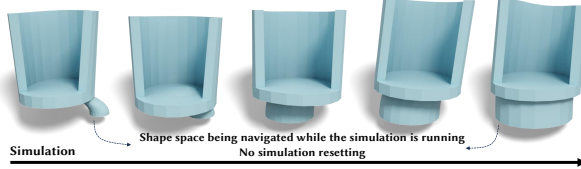


Fig. 11. *Interactive Manipulation*. Our method can recalculate the basis in real-time, enabling seamless shape changes during simulation.

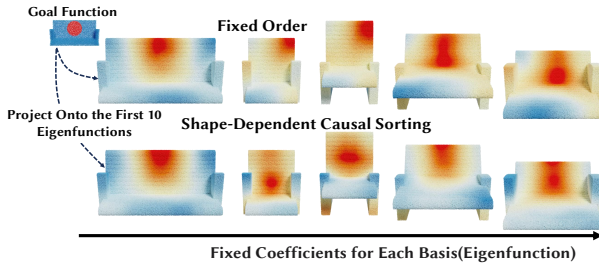


Fig. 12. *Information Transfer*. We evaluated the evolution of eigenfunctions on another family of shapes. Our method shows better consistency.

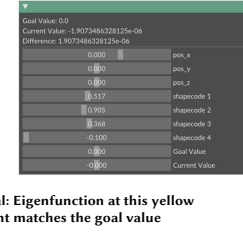


Fig. 13. *Inverse Design*. Our end-to-end differentiable framework supports gradient-based inverse design



Fig. 14. *Boundary Condition*. To visualize the boundary condition, isolines of the eigenfunctions are shown. Note that the gradient with respect to the boundary is close to zero.

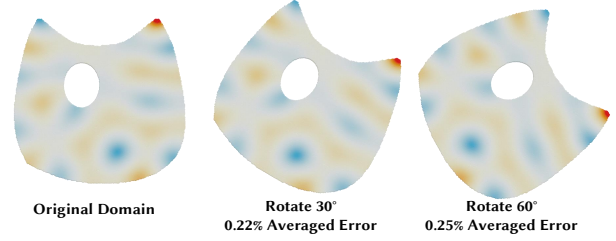


Fig. 15. *Error Evaluation for Rotation Perturbations*. We retrained the network on rotations of the same shape with different angles. Our method demonstrates high consistency under rotational perturbations. Specifically, for rotations of 30 and 60 degrees, the average error over the first 30 modes between the rotated and original domains is 0.22% and 0.25%, respectively. For context, variations within the 0.2% – 0.3% range frequently occur due to re-initializing network weights before training, indicating no significant bias for rotations. The 30th eigenfunction from the three training results is visualized in this figure.

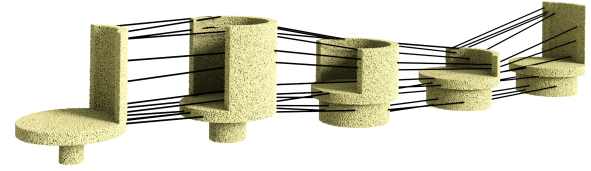


Fig. 16. *Correspondence within Shape Space*. Our method enables correspondence calculation within the shape space. The eigenfunctions, after being processed with shape-dependent causal sorting, can be directly used to calculate correspondences within the shape space. This eliminates the need to calculate additional functional maps for each pair of shapes within the family.